Supporting Information

A Carbonate-free, Sulfone-based Electrolyte for High Voltage Li-ion Batteries

Judith Alvarado[a,b,†], Marshall Schroeder[a,†], Minghao Zhang[b], Oleg Borodin[a], Eric Gobrogge[a], Marco Olguin[a], Michael Ding[a], Mallory Gobet[c], Steven Greenbaum[c], Ying Shirley Meng[c,*], Kang Xu[a,*]

E-mail: conrad.k.xu.civ@mail.mil

Table S1. Approximate Electrolyte conversions from molality to molarity.

LiFSI-SL and LiPF6-SL

Molality (m)	Molarity (M)
1.00m	1.26M
2.00m	2.52M
3.00m	3.78M
3.25m	4.10M
3.50m	4.41M
3.75m	4.73M

LiFSI-PC and LiPF6-PC

Molality (m)	Molarity (M)
1.00m	1.21M
4.00m	4.82M

Table S2. T_0 and activation energies from electrolyte conductivity measurements.

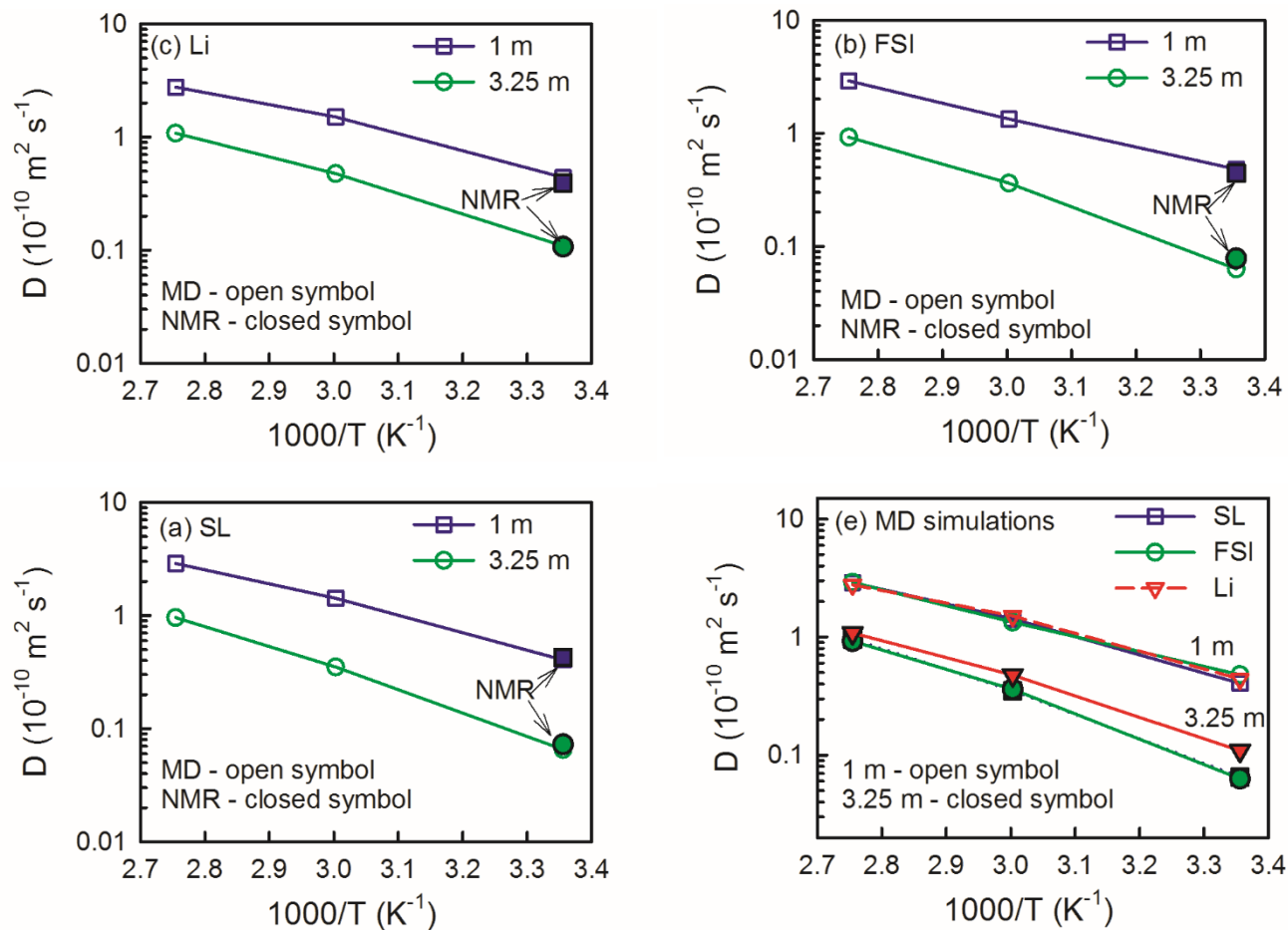| Electrolyte	T_0 (K)	E_a (kJ mol^{-1})
1.0m LiPF$_6$ (EC/EMC 3:7)	161	2.84
1.0m LiFSI-SL	130.6	6.59
3.25m LiFSI-SL	146.8	7.1

Figure S1. Solvent (SL) and ion self-diffusion coefficients from MD simulations at 363 K, 333 K, 298 K and NMR measurements at 298 K.
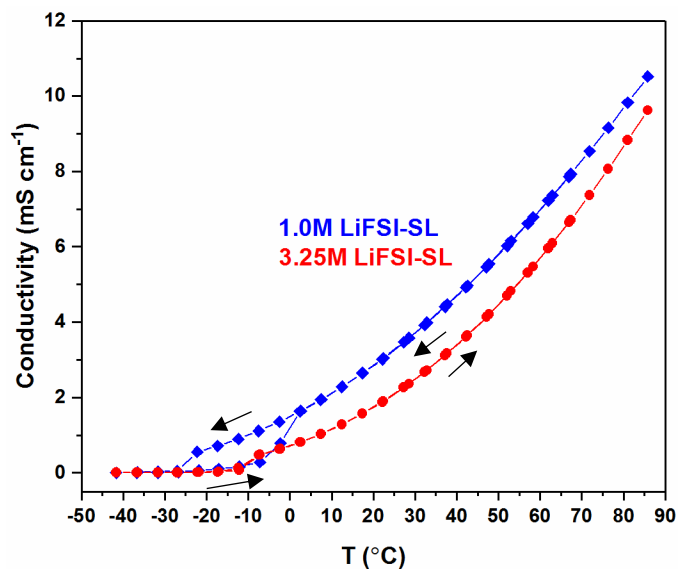

Figure S2. Conductivity curves of low and high concentration LiFSI-SL electrolytes. Measurements were taken in 5°C increments from 85 to -20°C, stopping at each for an hour of thermal equilibrium before measuring conductivity. See experimental section for more information.
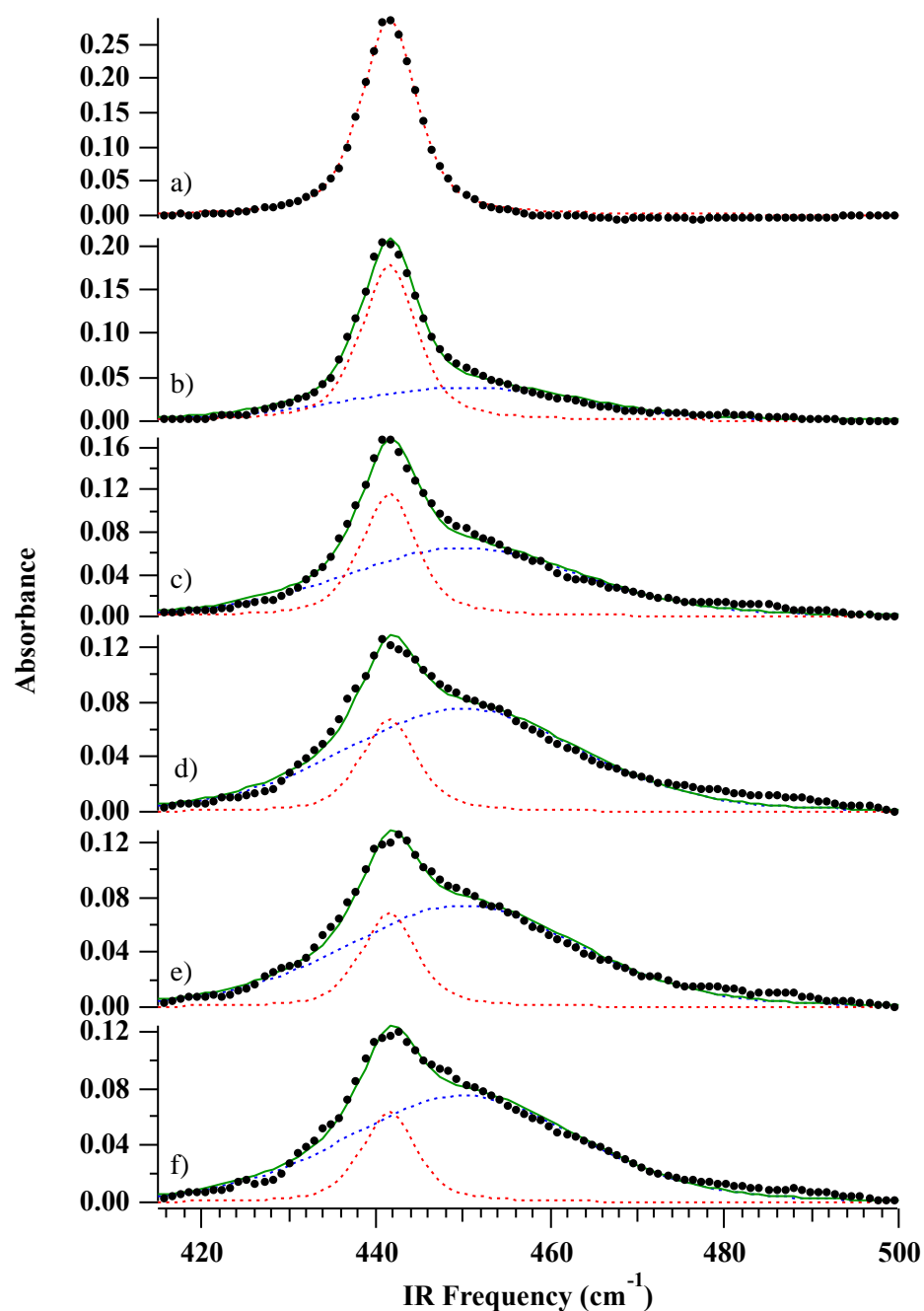
Figure S3. FTIR spectra of sulfolane's SO_2 twist in different LiFSI/SL mixtures (a: 0 m, b: 1 m, c: 2 m, d: 3.25 m, e: 3.5 m, f: 3.75 m). Experimental spectra are designated by black markers, and the corresponding fits are shown as green lines. Deconvoluted components are indicated as red dashes (non-solvating SL component) and blue dashes (Li^+ solvating SL).
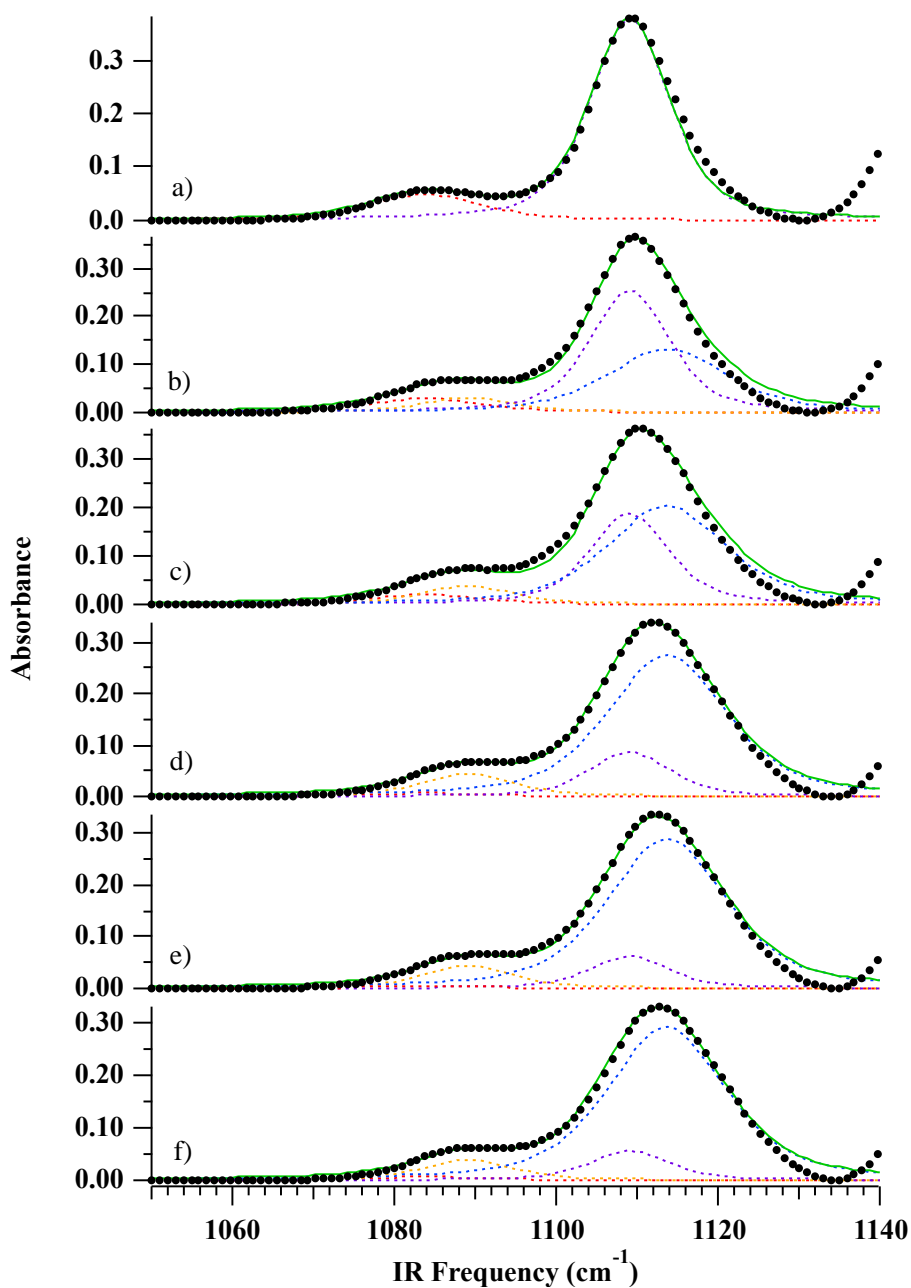
Figure S4. FTIR spectra of sulfolane's CH_2 vibrations in different LiFSI/SL mixtures (a: 0 m, b: 1 m, c: 2 m, d: 3.25 m, e: 3.5 m, f: 3.75 m). Experimental spectra are designated by black markers, and the corresponding fits are shown as green lines. Deconvoluted components are indicated as red and purple dashes (non-solvating SL component), and orange and blue dashes (SL solvating Li^+).

The CH_2 region of SL/LiFSI mixtures is more complicated but can be deconvoluted into four components (Figure S2). The features at 1085 cm^{-1} and 1108 cm^{-1} represent CH_2 vibrations in non-solvating SL molecules whereas the features at 1090 cm^{-1} and 1114 cm^{-1} represent the same vibrations in solvating SL molecules.
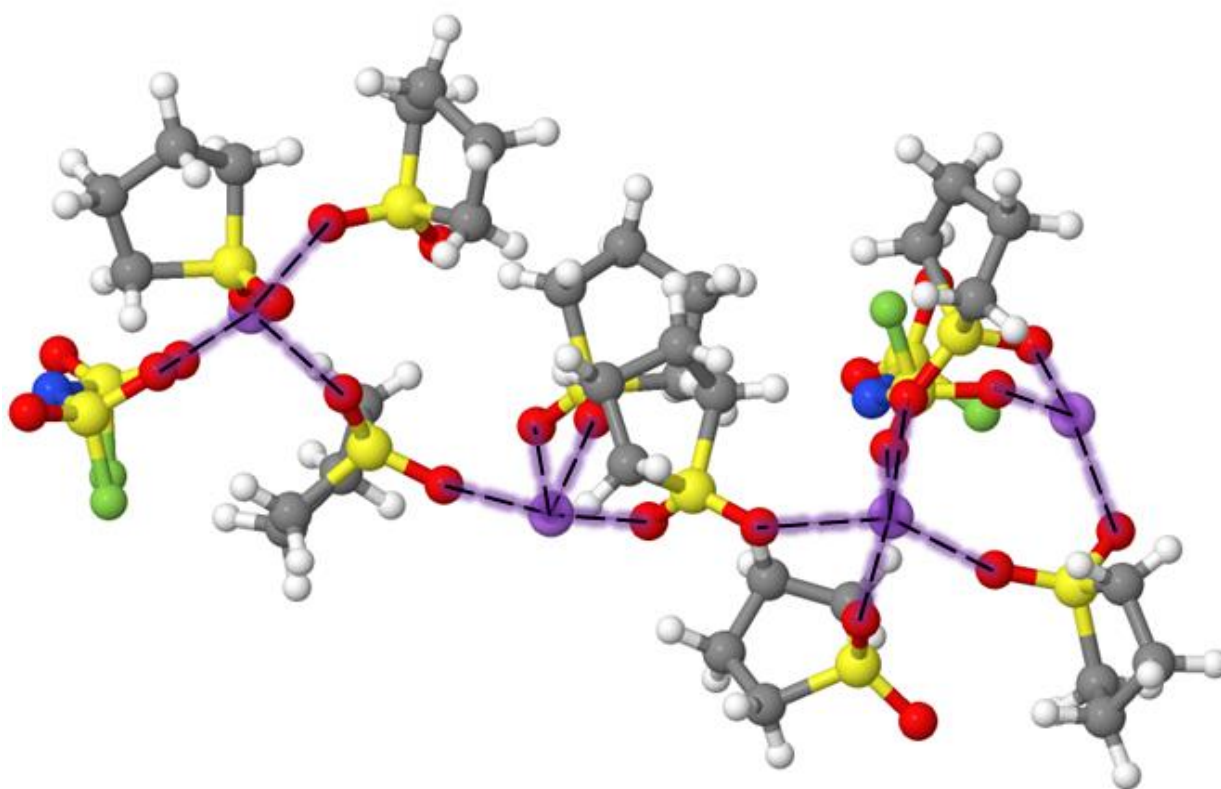
Figure S5: Model of extended aggregate showing an extensive oxygen bridging network between multiple SL molecules.
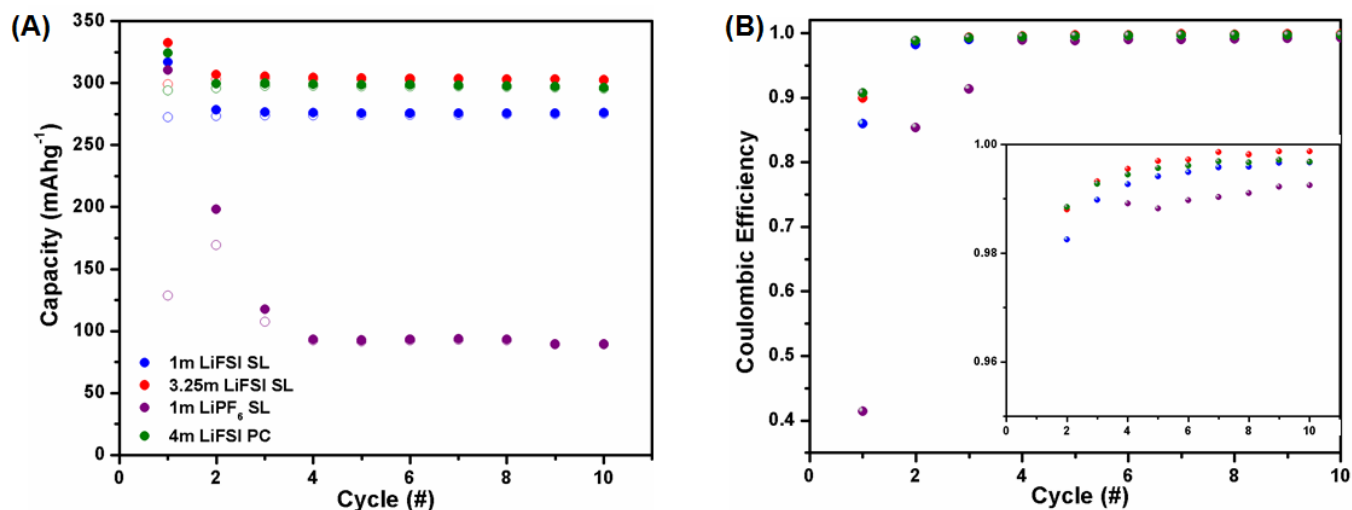
Electrochemical Analysis

Figure S6. Galvanostatic cycling of MCMB half cells (A) and coulombic efficiency (B) comparison for propylene carbonate and sulfolane electrolytes.
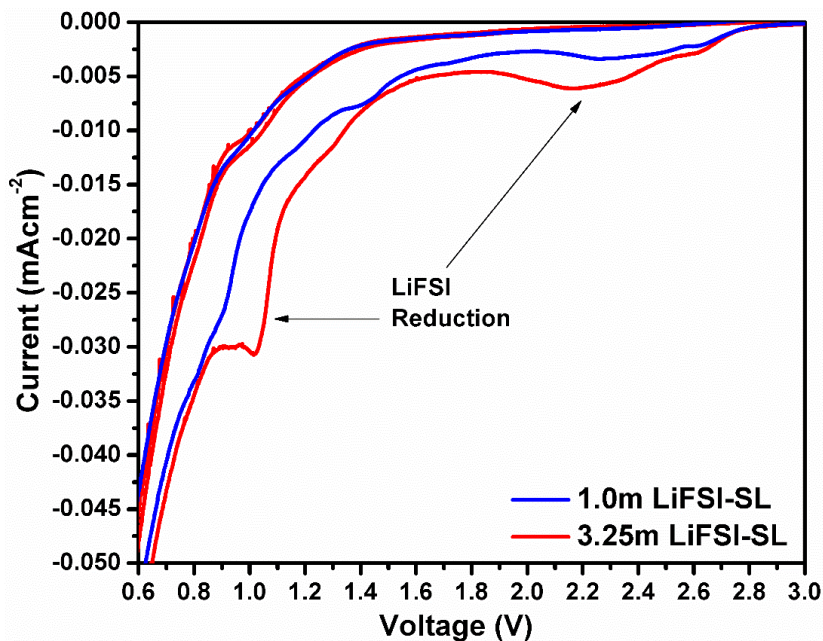
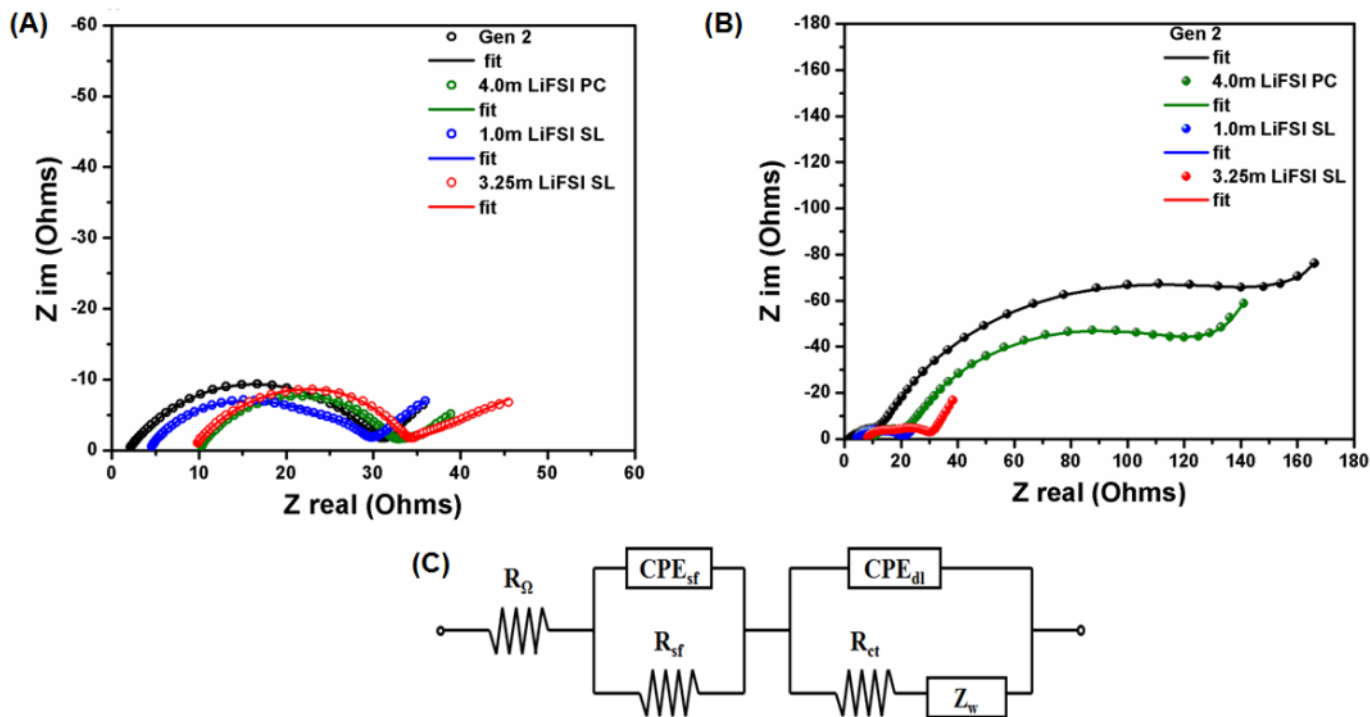Figure S7. Magnified CV of Figure 3D of main text, showing the decomposition peaks of LiFSI.

Figure S8. Electrochemical impedance spectroscopy measurements of cycled MCMB graphite half cells at the (A) lithiated and (B) delithiated state of charge. (C) Corresponding equivalent circuit used to fit the Nyquist plot.

Table S3. Impedance values after the lithiated state.

Symbol	Gen II	4.0m LiFSI PC	1.0m LiFSI SL	3.25m LiFSI SL
R_Ω	1.804	9.991	4.275	9.382
R_{sf}	19.77	12.19	21.78	8.619
R_{ct}	9.766	8.935	3.202	14.43
Chi value	3.63×10^{-5}	1.44×10^{-5}	4.49×10^{-5}	9.73×10^{-5}

Table S4. Impedance values after the delithiated state.

Symbol	Gen II	4.0 m LiFSI PC	1.0 m LiFSI SL	3.25m LiFSI SL
R_Ω	1.768	9.47	4.147	7.86
R_{sf}	12.09	13.04	11.16	9.515
R_{ct}	167.9	123.7	4.257	13.44
Chi value	1.47×10^{-4}	4.84×10^{-5}	7.20×10^{-5}	1.06×10^{-5}

Tables S3, S4 show the changes in the impedance of the MCMB graphite half cell after the first lithiation (Table S3) and delithiation (Table S4). The measurements took place in the same cell to not disturb the natural cycling environment. Impedance spectroscopy produces a Nyquist plot which reveals real part of the measured impendence versus its imaginary component over a range of AC frequencies. A circuit was modeled after the reactions that occur during electrochemical cycling, to properly quantitatively analyze the data. The model accounts for the uncompensated Ohmic resistance of electrolyte (R_Ω), the double layer capacitance of the electrode/electrolyte interface (CPE_{sf}), resistance due to the surface reactions on the electrode (Rf), the double-layer capacitance (CPE_{dl}), the charge transfer resistance (Rct), and the impedance due to solid state diffusion processes, known as the Warburg impedance (Zw). The corresponding values are shown in table 1 and 2.
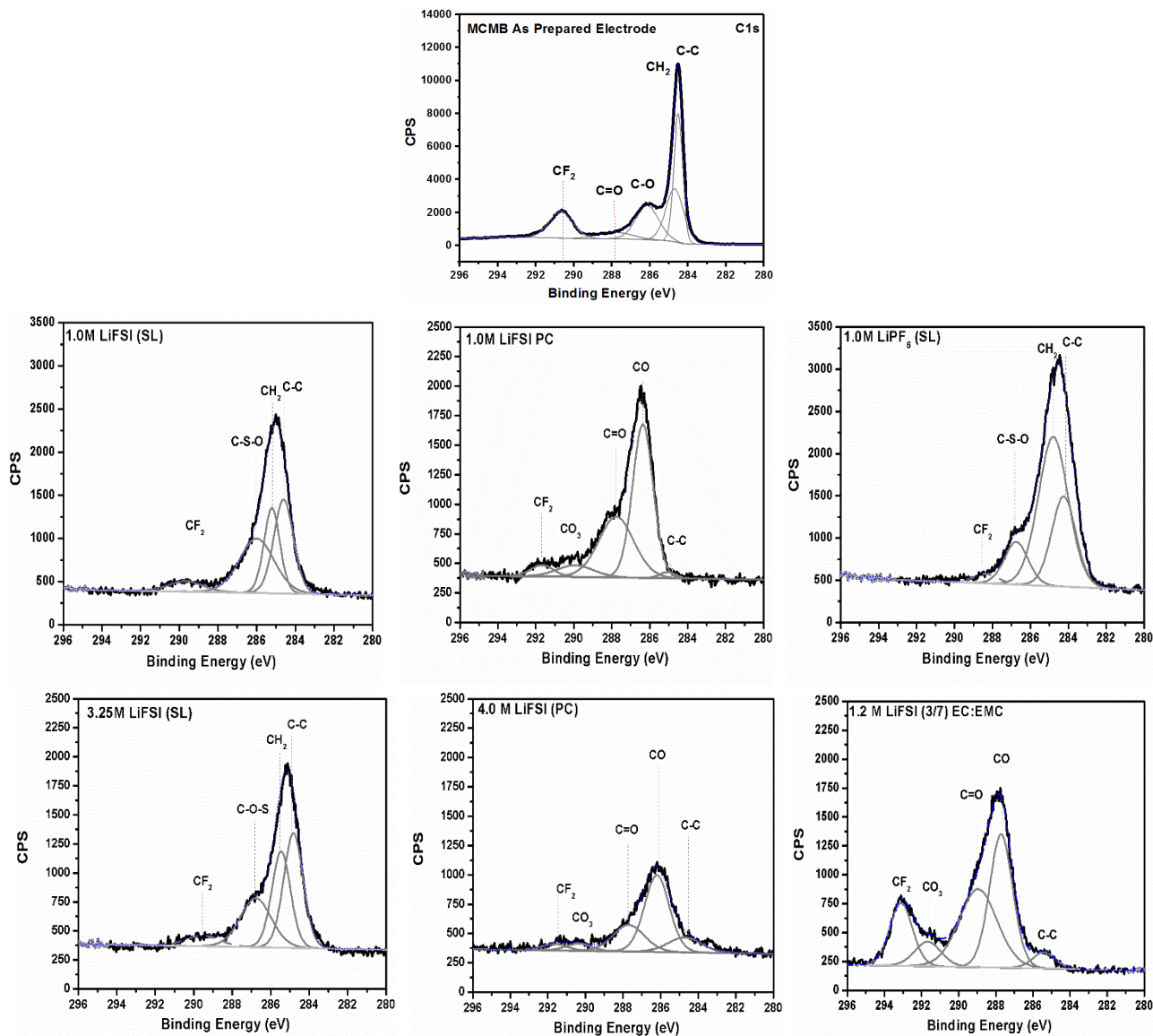
XPS Analysis

Figure S9. XPS C1s spectra for the as prepared MCMB graphite electrde (top) and cycled electrodes after the fifth discharge.

The as-prepared electrode contained peaks that correspond to graphite (284.51eV), conductive additive (286.13eV) and PVDF binder (290.67eV). The contribution of the binder can be seen in all the electrodes, regardless of electrolyte used. The graphite anodes cycled in low and high LiFSI concentrations in SL have two main peaks associated to the decomposition of SL. The peak at 285.2 eV is due to the alkyl carbons in the SL, while the peak at 286.5 eV results from C-S-O bond. We can also see a small peak associated to the PVDF binder, 289.6 eV. Given that we use a two component system and the stability of SL towards graphite, the C 1s spectra is relatively simple. This can is also seen in the cell cycled with 1.0m LiPF$_6$-SL electrolyte. At 1.0m LiFSI-PC, the SEI is attributed to the reduction products of PC (CO, OCO, CO$_3$)[1], which is evident by the measured counts-per-second (cps). However, once the salt concentration increases, the signals for organic moieties decrease significantly owing to a system that is driven by salt decomposition rather than solvent.[2] The graphite anode cycled with 1.2m LiFSI EC:EMC (3:7) contained high amounts of carbonate species due to the reduction of EC.[3]
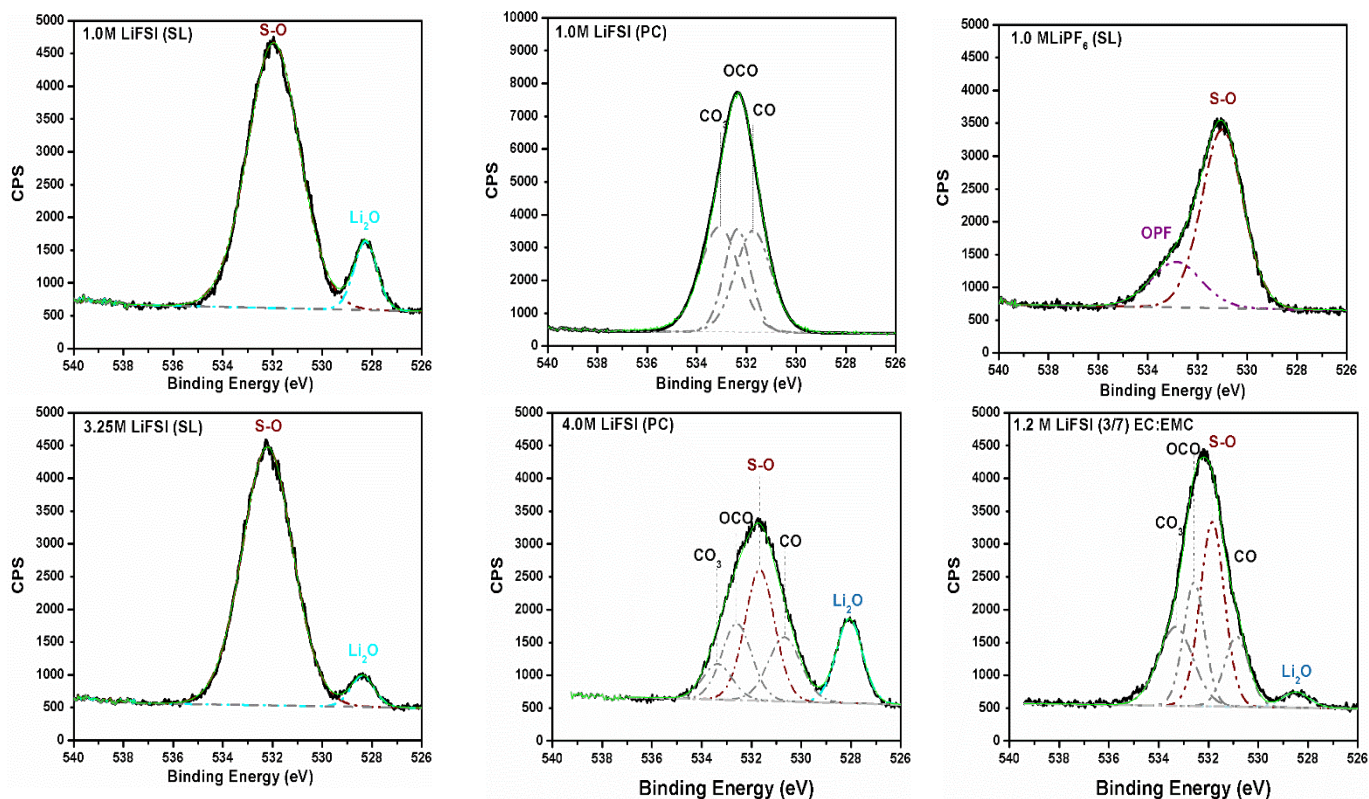
Figure S10. XPS O1s spectra for the cycled electrodes after the fifth discharge.

Consistent with the C1s, the electrodes cycled with SL have a decomposition peak corresponding to the sulfur-oxygen bond. This peak can also correspond the decomposition of the LiFSI salt. More importantly, the peak at 528.3 eV is attributed to Li_2O as discussed in the main text, which can also be seen in all the electrodes that were cycled with LiFSI. This result suggests that the Li_2O is most likely related to decomposition of the FSI$^-$ anion. The O1s correlates well with the C1s, where we can see that at high concentrations of LiFSI in PC there is a signal due to the salt primarily decomposing (3500 cps for 4.0m LiFSI-PC vs 8000 cps for 1.0m LiFSI PC). When the graphite is cycled with 1.0m $LiPF_6$-SL, the O1s spectrum is primarily composed of S-O peaks and OPF which is the result of the decomposition of the salt to from $Li_xO_yPF_x$.[4]
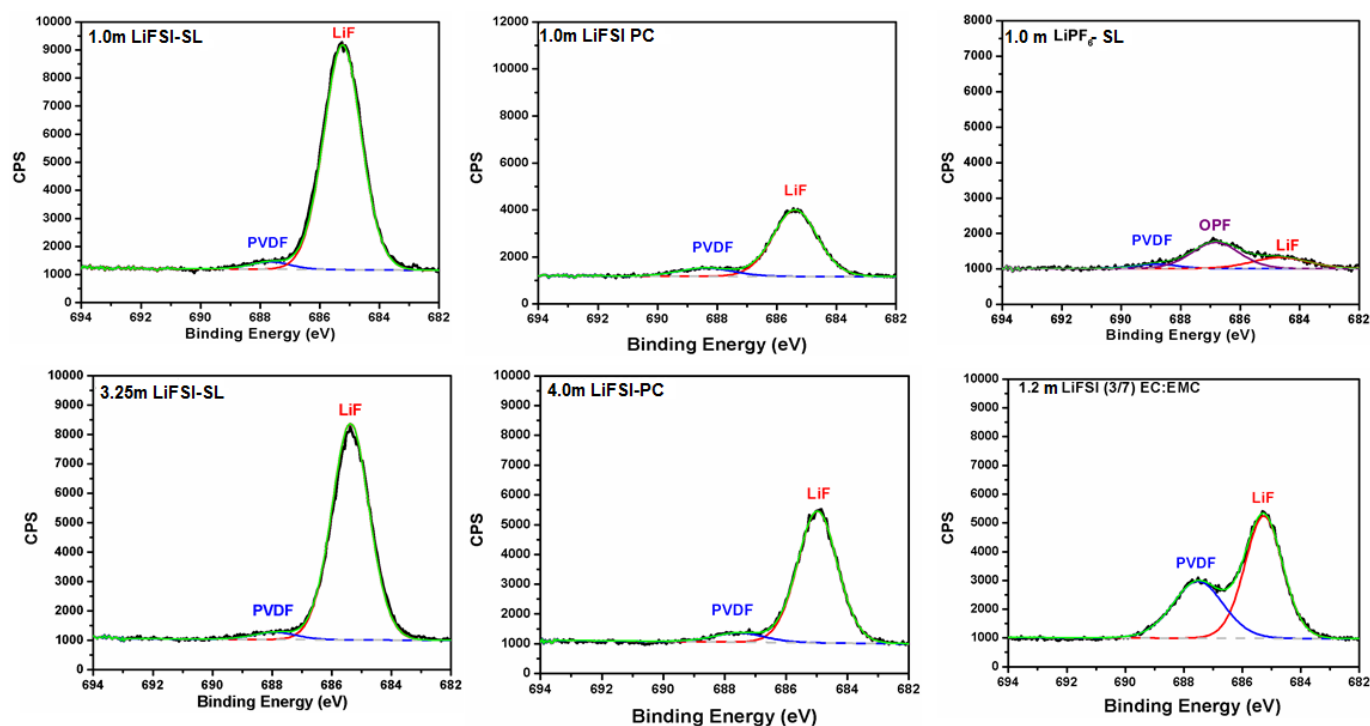
Figure S11. XPS F1s spectra for the cycled electrodes after the fifth discharge.

Given that our electrolyte consists of LiFSI-SL, the low and high concentrations have a very similar SEI (seen in all the XPS spectra)—and the F1s spectra is no exception. The spectra for both SL electrolytes is predominantly the LiF signal with a very small signal of PVDF, as discussed in the main text. When the spectra is not normalized, as in the main text, the ratio between LiF and PVDF becomes more apparent. More importantly, for the 4.0m LiFSI-PC the LiF signal increased from 4050 cps to 5600 cps which is consistent with an SEI the contains high salt decomposition and less solvent functionalities. Although 1.0m LiPF6-SL cycles graphite reversibly, albeit at 50% capacity of graphite, the SEI composition gleans some insight as to why this occurs. This could be due to the lack of inorganic species (LiF and Li_2O), as the signal for the $Li_xO_yPF_x$ (OPF) and LiF is below 1790 cps. When $LiPF_6$ in Gen II salt is swapped with LiFSI, the percent concentration of LiF is 61.78% to 38.22% PVDF. The solvation properties of EC and EMC allows for the salt to decompose on the surface of the graphite anode.
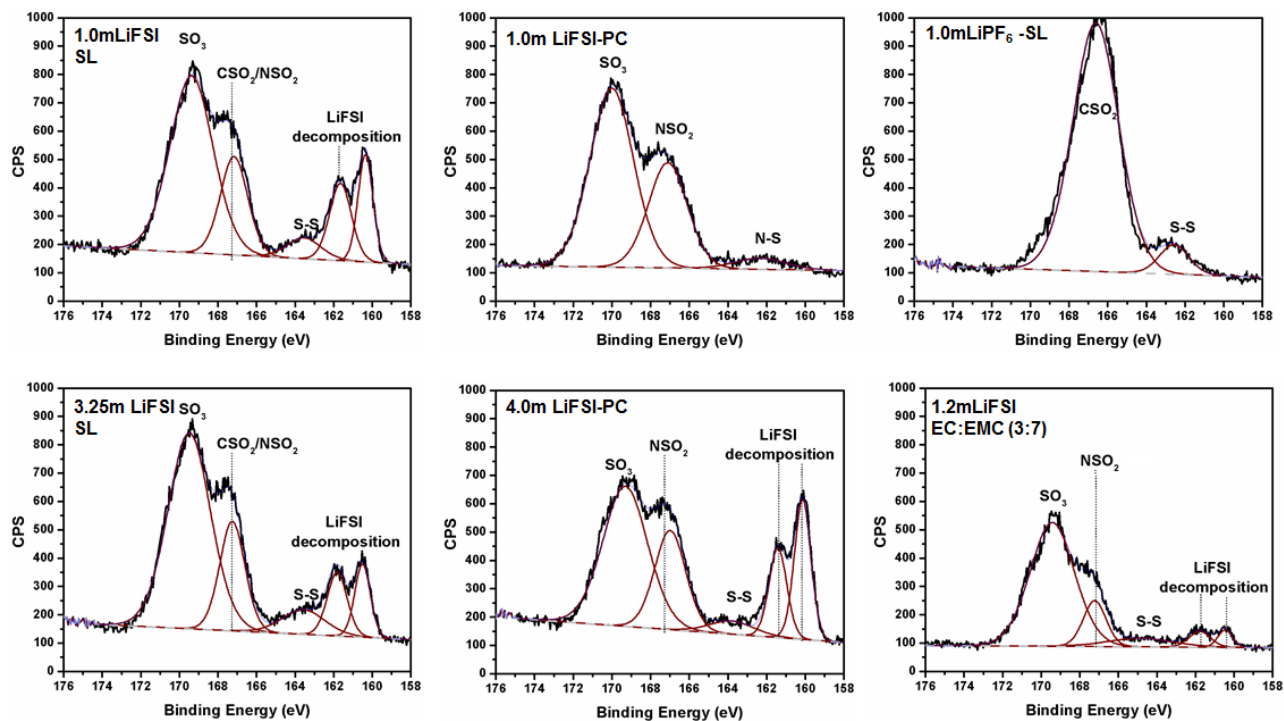
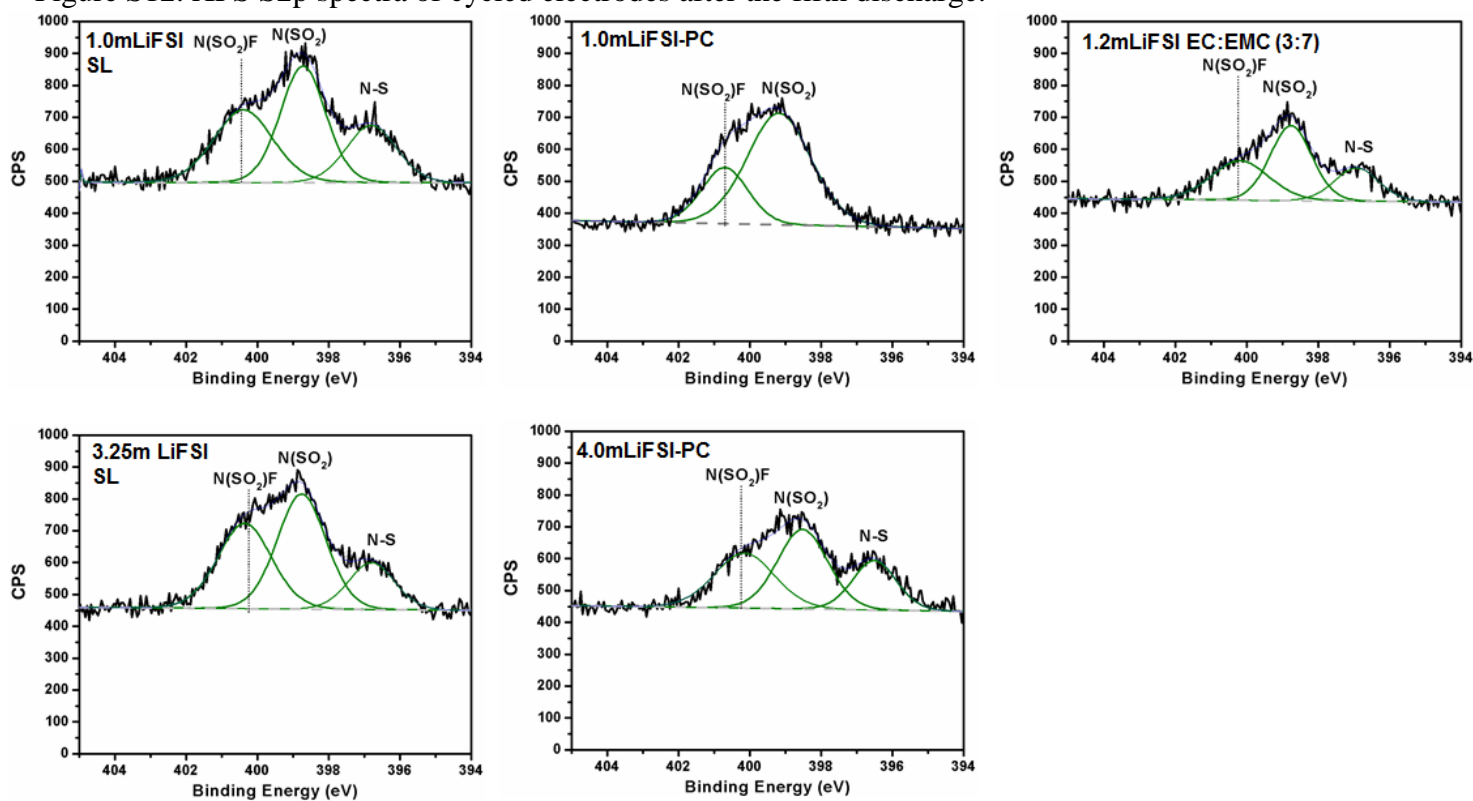Figure S12. XPS S2p spectra of cycled electrodes after the fifth discharge.

Figure S13. XPS N1s spectra of cycled electrodes after the fifth discharge.

Both Figures S10 and S11 focus on the decomposition of the LiFSI salt. In Figure S7 we have attempted to isolate the peaks that are associated with salt and solvent reduction as a result of deliberately characterizing/comparing SEIs from specific electrolytes (LiPF$_6$-SL and the LiFSI containing electrolytes (top right in Figure S9 and S10). Here we can see in the S2p spectra that the peaks are only associated to the SL decomposition, consisting pf CSO$_2$ (166.62 eV) and S-S(162.53 eV).[5] We note that Li$_2$SO$_3$ is not formed from the decomposition of SL, as stated by Li et al.[6] However, the SO$_3$ functionality is found in the electrodes cycled with LiFSI containing electrolytes. Therefore, it is possible that the SO$_3$ functionality may be the result of subsequent LiFSI decomposition reactions. Moreover, the CSO$_2$ peak overlaps with NSO$_2$ (~167.2 eV) that occurs from LiFSI reduction. The peaks at higher binding energy are consistent with the literature associated with LiFSI.[7] However, for the first time, we attribute peaks at ~161.3 eV and 160.5 eV to be from the LiFSI decomposition products, which is not seen in the literature and in the SEI generated from LiPF$_6$-SL. The corresponding decomposition products are shown in Figure S11 which correlate well with the S2p spectra.
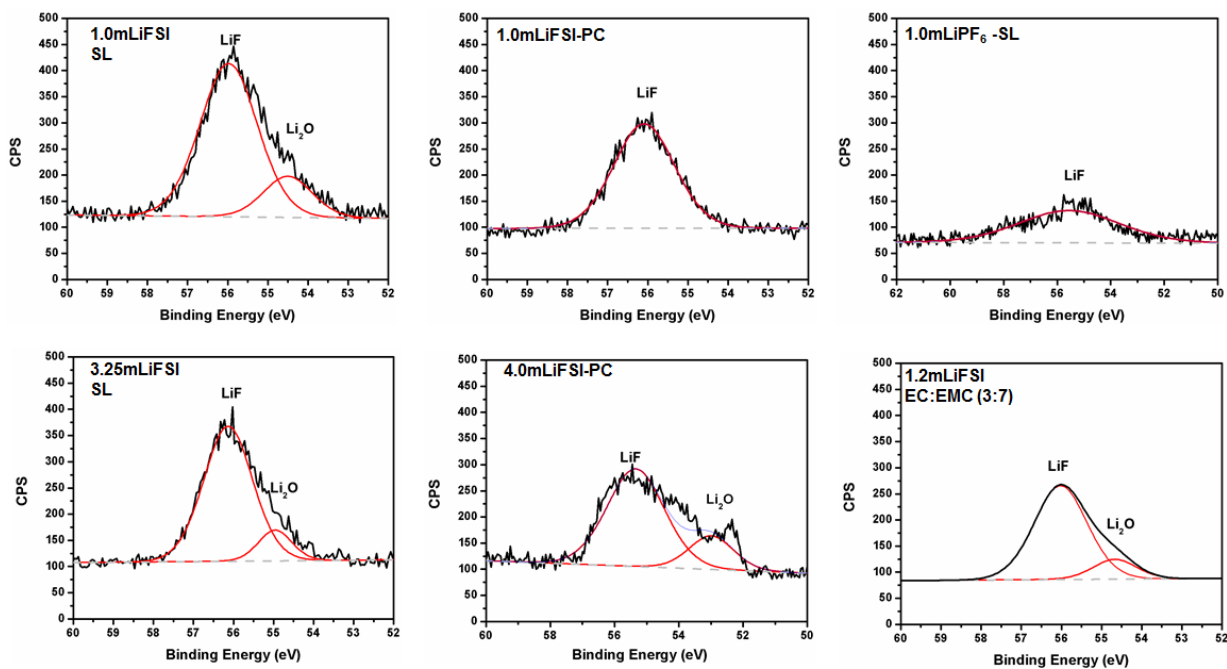

Figure S14. XPS Li1s spectra of cycled electrodes after the fifth discharge.

Figure S12 shows that the Li 1s spectra shows LiF between 55.8eV-56 eV for all electrolytes. Consistent with the O1s, we see a peak at ~ 54.5 eV associated with lithium oxide. The electrodes that had the worst electrochemical performance (Figure S4), contained less LiF and no lithium oxide in their SEI (1.0m LiFSI-PC, 1.0m LiPF6-SL).
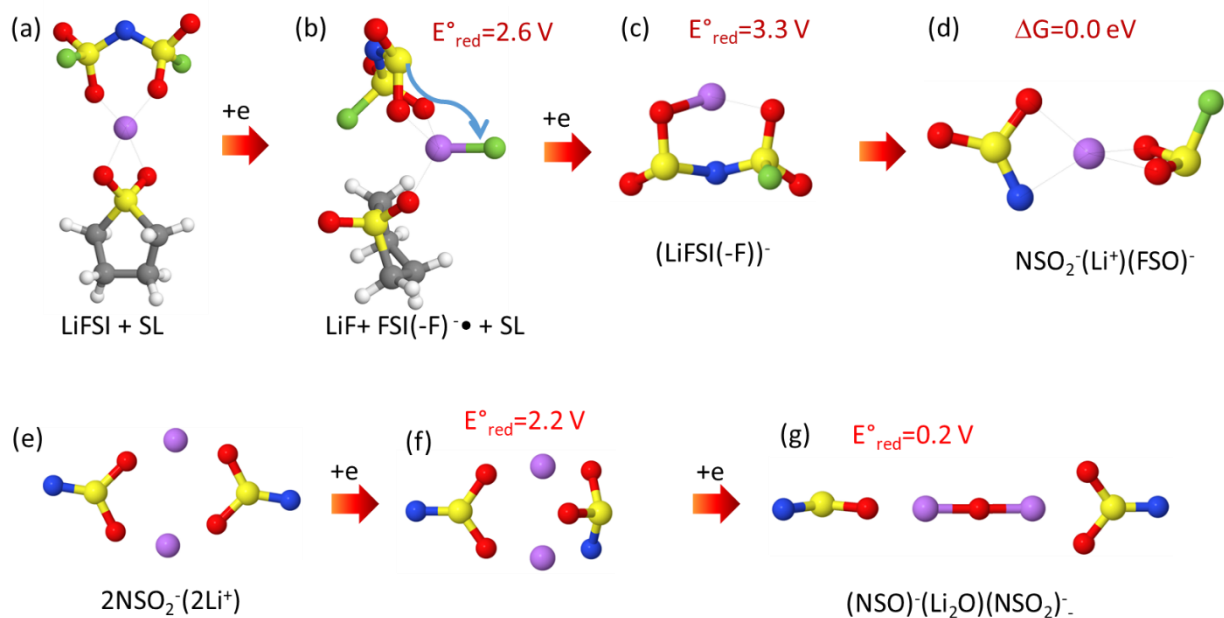
Figure S15: Reduction pathway and associated stepwise energetics from G4MP2 QC calculations for the formation of Li_2O from LiFSI and SL using SMD(SL) implicit solvent model for (a-b) and previous results[8] (c-g) using SMD(ether) model.
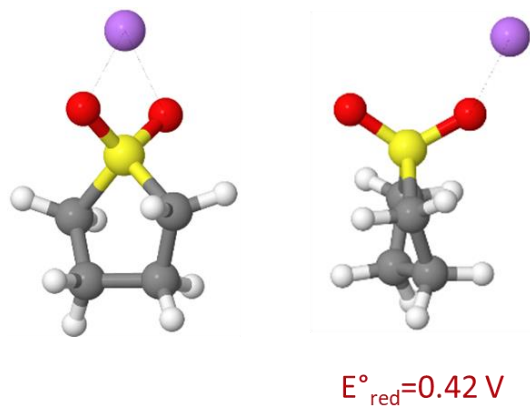

Figure S16: Reduction potential for SL in the presence of Li from G4MP2 with SMD(SL) QC calculations.
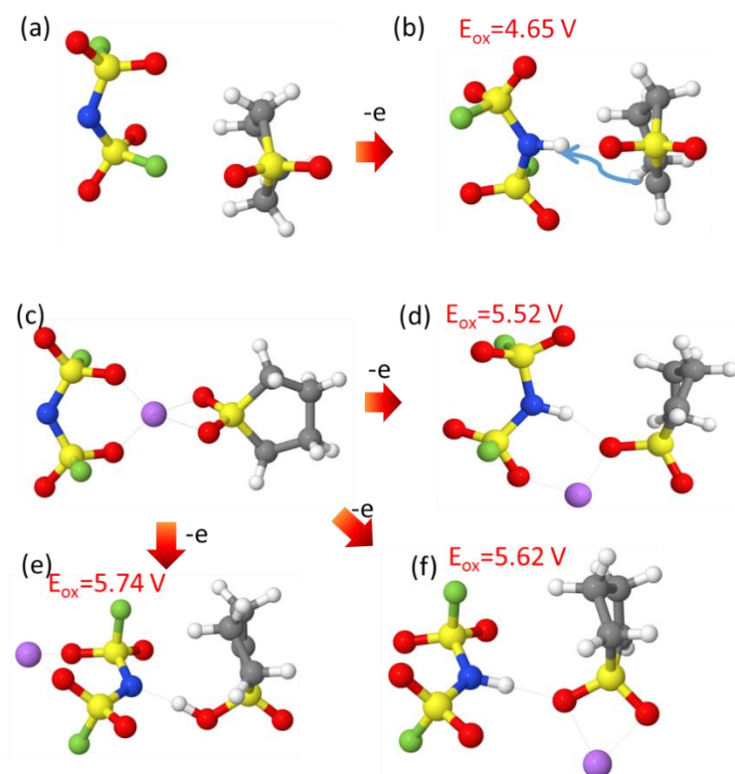
Figure S17: Expanded version of Figure 4 from the main text. Oxidation potential (vs. Li/Li+) from G4MP2 QC calculations with clusters surrounded by SMD(SL) implicit solvent model.
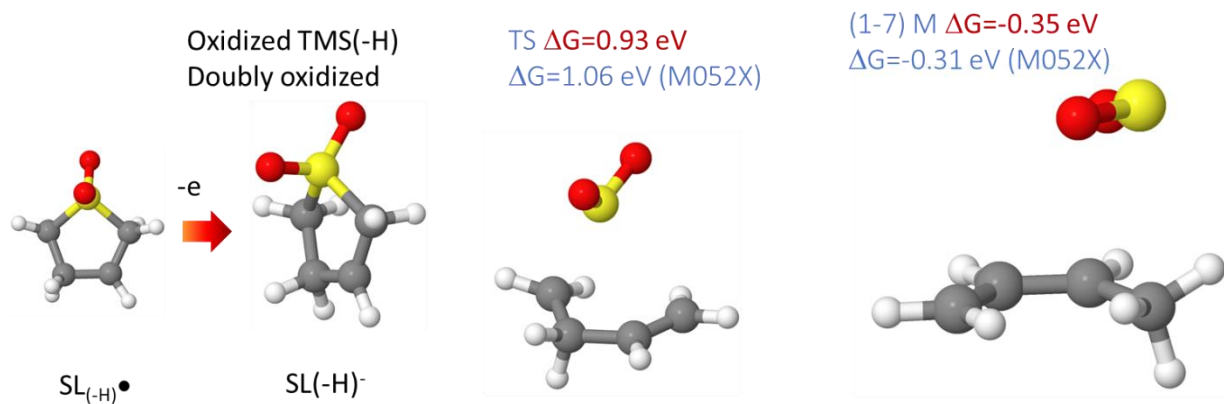

Figure S18: Calculations showing SO_2 evolution resulting from a second oxidation of SL from G4MP2 (shown in red) and M05-2X/6-31+G(d,p) (in blue) calculations with SMD(SL) implicit solvation model.

(a) Li+(PC)
ΔE=-49.4 kcal/mol
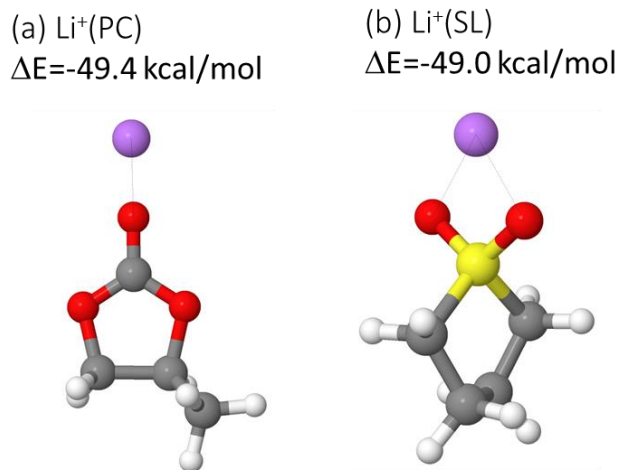
(b) Li+(SL)
ΔE=-49.0 kcal/mol

Figure S19: Comparison of PC and SL binding energies to Li from calculations with SMD(SL) implicit solvation model.
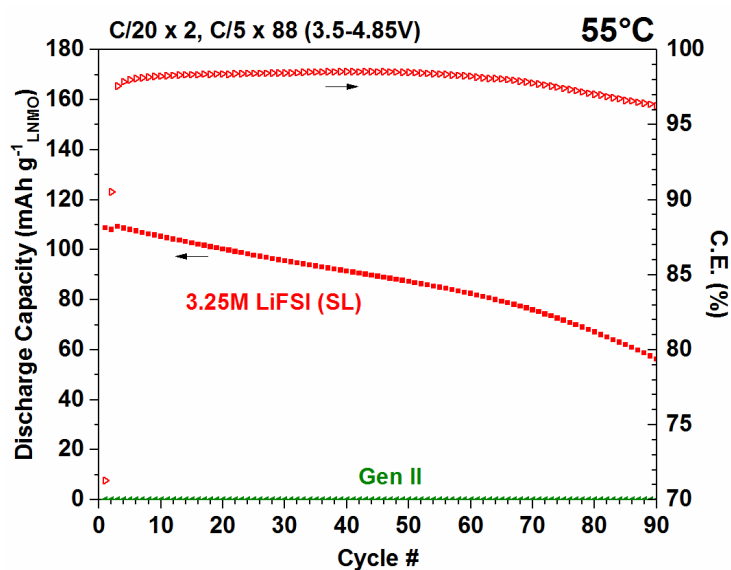

Figure S20: High temperature (55°C) cycling data comparing high concentration LiFSI-SL with the baseline carbonate (Gen II) in a LNMO-MCMB full cell. Cycling parameters (C/20 x 2, then C/5 from 3.5-4.9V)
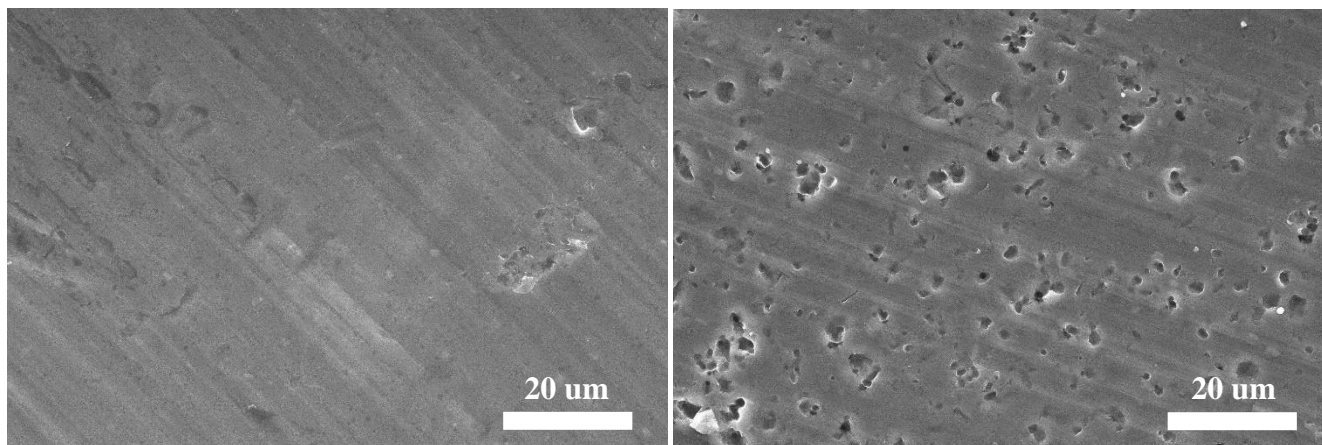
Figure S21: Backside (left) and active material side (right) SEM images of Al cathode current collector after 1000 cycles showing significant differences in corrosion levels.
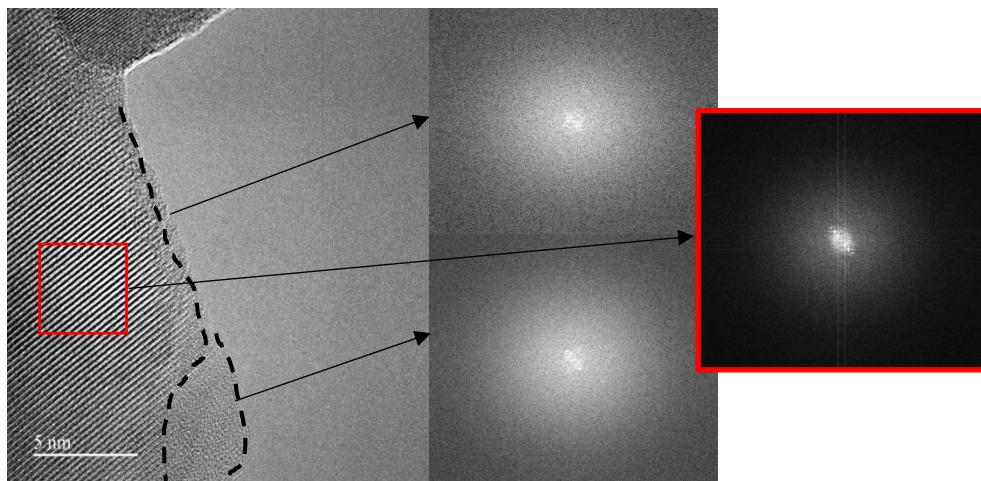
Figure S22: TEM of LNMO particle cycled in carbonate baseline (Gen II) with CEI that varies in thickness. The FFT pattern indicates that the CEI is amorphous, with the FFT pictured in the red box confirming the crystallinity of the LNMO particle in the (003) plane.

Figure S23: TEM of LNMO particle cycled in 3m LiFSI-SL with a uniform CEI. The FFT pattern indicates that the CEI is amorphous, with the FFT pictured in the blue box confirming the crystallinity of the LNMO particle in the (113) plane.

Figure S24. EELS spectra of the sulfur L-edge of the LNMO CEI after 50th discharge when cycled with 3m LiFSI-SL.

Figure S25: Normalized EELS spectra of the O K-edge and the Mn L3/L2 edges.

Figure S26: DSC plots of 3.25m LiFSI-SL and Gen 2 electrolytes with anode and cathode cell fragments in the charged state.
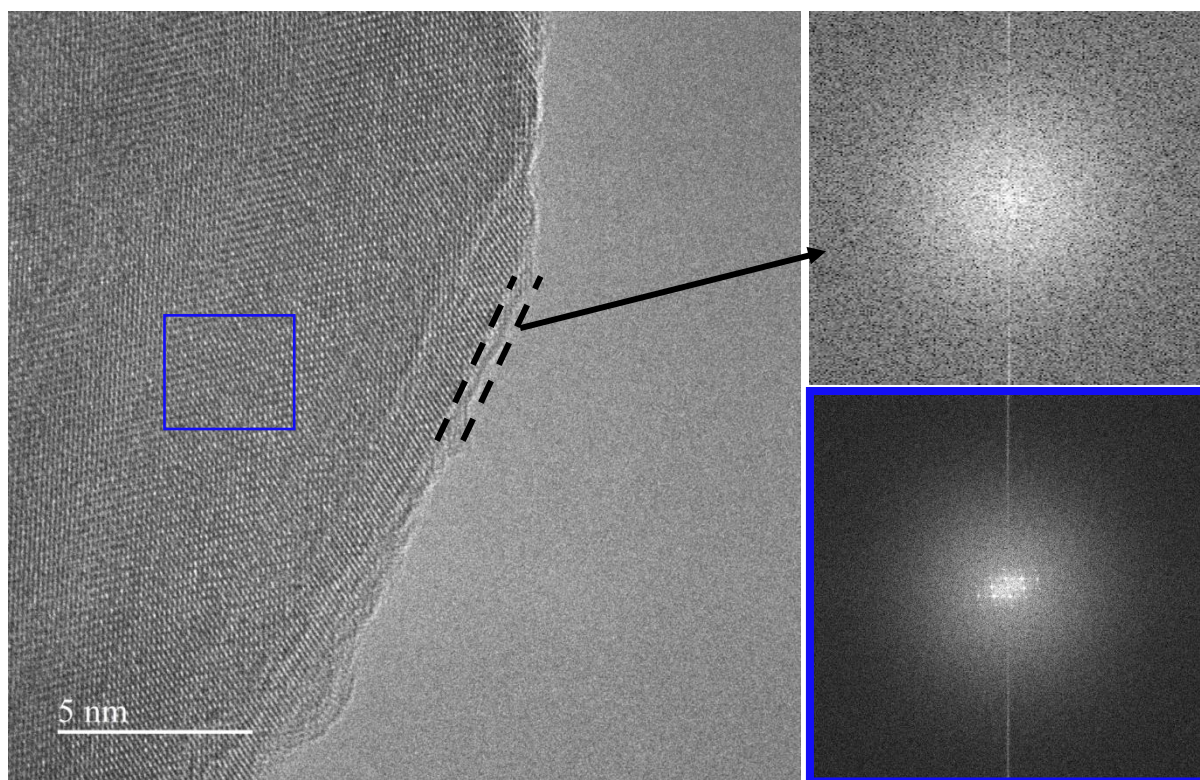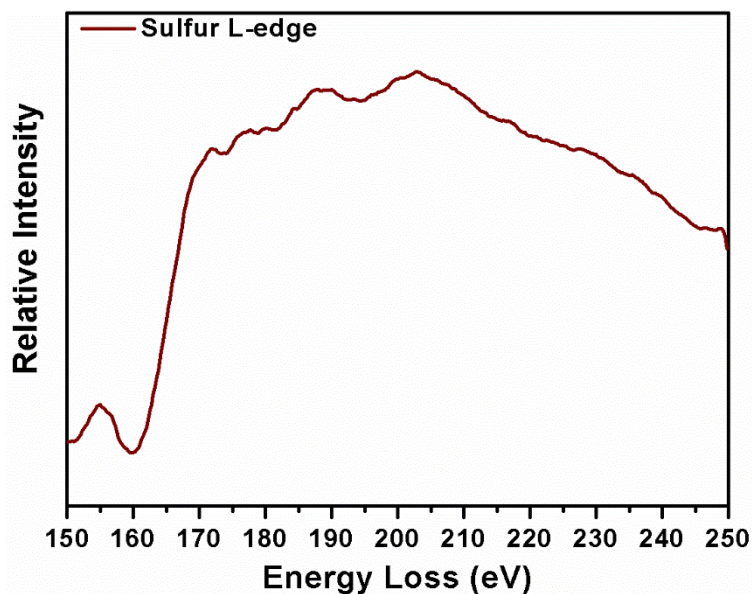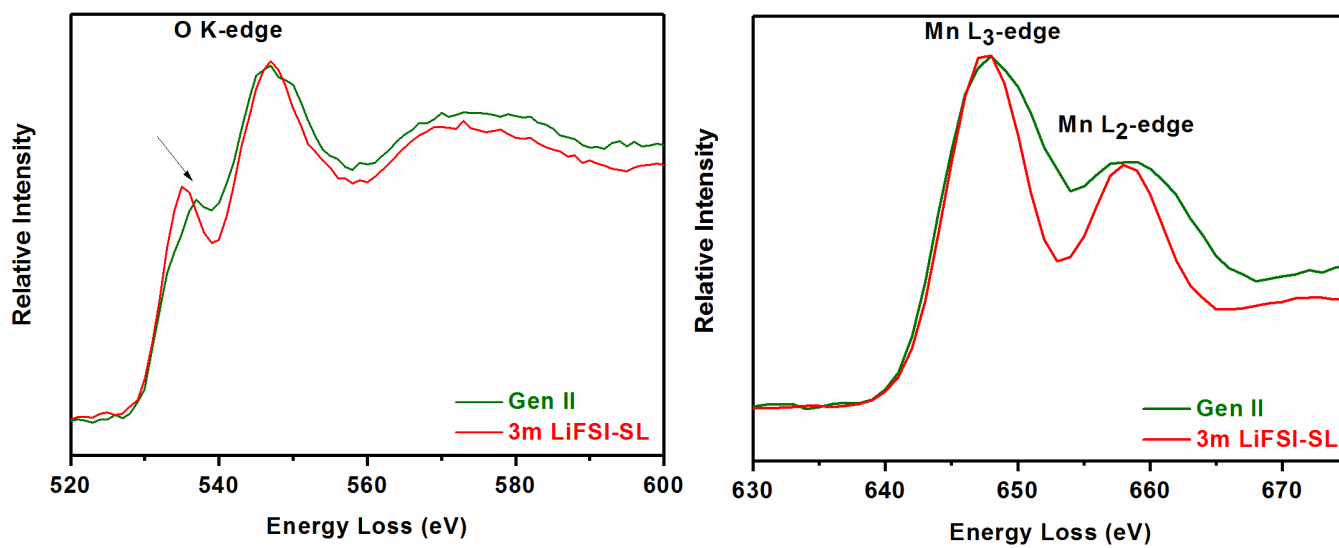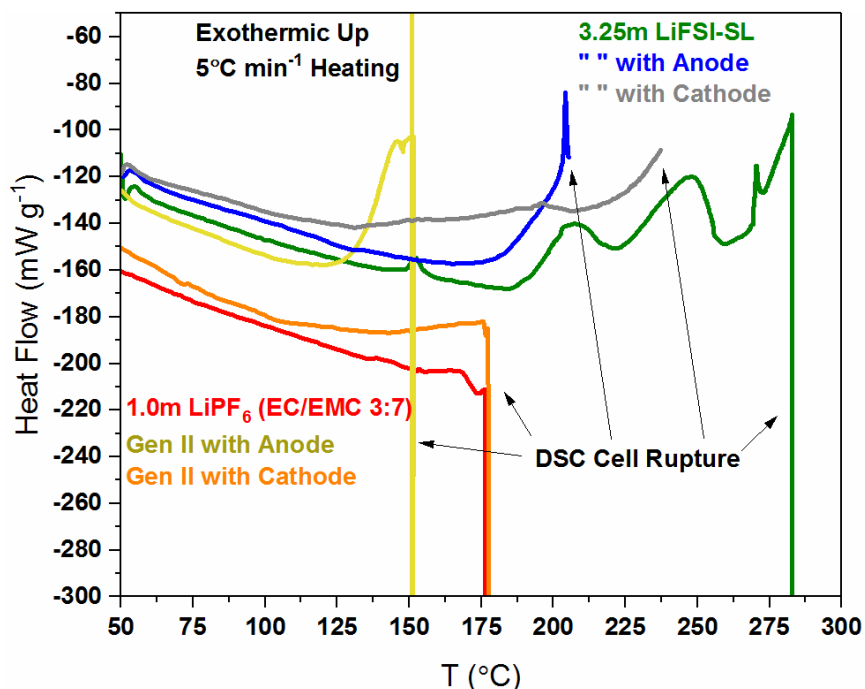
The safety of the SL-FSI system was preliminarily evaluated by differential scanning calorimetry (DSC) using fully-charged cathode and anode fragments recovered from cycled LNMO-MCMB full cells in presence of as-prepared Gen II or 3.25 m LiFSI-SL electrolyte. The low thermal stability of Gen II electrolyte was clearly indicated by the early cell rupture at low temperature when charged LMNO reacts with the carbonate. SL electrolyte mixture with the charged cathode exhibits no major thermal event until 225°C during an exothermic process, suggesting the electrolyte is stable at high temperatures even in the presence of the typically highly reactive charged cathode surfaces. This is in part due to the high thermal inertness of both salt (LiFSI) and solvent (SL), as compared to the thermally reactivity between $LiPF_6$ and carbonate solvents.[9, 10]

Molecular Dynamics Simulations

Molecular dynamics (MD) simulations were performed on the LiFSI-SL electrolytes at two compositions: 1m and 3.25m at 363 K, 333 K and 298 K. The simulation cell contained 400 SL, 48 LiFSI for 1m and 320 SL and 125 LiFSI for 3.25m. All simulated systems were created in a gas-phase resulting in the large simulation cells of ~80 Å. The simulation box dimensions were gradually decreased to ~45 Å at 500 K. Next, NPT equilibration runs were performed at 393 K for 3 ns for 1m and 6 ns for 3.25m. After that the temperature was decreased to

363 K and MD simulation runs were performed in the NPT ensemble. After NPT equilibration runs at 363 K, the temperature was further reduced to 333 K and NPT equilibration runs were performed at 298 K. Production runs were performed in the NVT ensemble using densities obtained from the last 4 ns of the equilibration runs. The lengths of production and equilibration trajectories are given in Table S5.

The Ewald summation method was used for the electrostatic interactions between permanent charges with permanent charges and permanent charges with induced dipole moments with $k = 6^3$ vectors. Multiple timestep integration was employed with an inner timestep of 0.5 fs (bonded interactions), a central time step of 1.5 fs for all nonbonded interactions within a truncation distance of 7.0-8.0 Å and an outer timestep of 3.0 fs for all nonbonded interactions between 7.0 Å and the nonbonded truncation distance of 19-20 Å. The reciprocal part of Ewald was updated only at the largest of the multiple time steps. A Nose-Hoover thermostat and a barostat were used to control the temperature and pressure with the associated frequencies of 10^{-2} and 0.1×10^{-4} fs. The stress tensor was saved every 3 fs for calculating stress, the tensor autocorrelation function, and viscosity, while the atomic coordinates were saved every 2 ps for post-analysis. Transport properties were calculated as discussed in previous publications.[11, 12]

A many-body polarizable force field (APPLE&P) with the previously described functional form was used.[13] The Li^+/FSI^- non-bonded force field parameters were largely taken from previous work on LiTFSI-H_2O.[12] The remaining parameters were fit to describe the Li^+/FSI^- binding energy obtained from G4MP2 calculations. The LiFSI(cis)/Li^+ and LiFSI(trans)/Li^+ binding energies were 134.8 kcal/mol and 135.9 kcal/mol from calculations using force field parameters compared to the same binding energies of 134.9 kcal/mol and 136.8 kcal/mol from G4MP2 calculations. The Li^+/FSI^- binding energies are similar to the energies obtained from the complete basis set extrapolation at MP2 level.[14] FSI(cis) and FSI(trans) denote the cis and trans conformations of F-S…S-F. In accord with our finding for concentrated LiTFSI-H_2O electrolytes, we find that description of ion dynamics is significantly improved when the Li^+ and TFSI charges were reduced by 6%. Therefore, we reduced the Li^+ cation and O(FSI^-) charges to yield ion charge of 0.94e. Reduction of the charges decreased the Li^+/FSI^- binding energy by ~19 kcal/mol in gas-phase. In order to balance the lower Li^+/FSI^- binding energy in the

Li$^+$(SL)$_3$FSI$^-$ solvates, the exp-6 repulsion parameters for Li$^+$/TMS were fit to the binding energy of 49.4 kcal/mol from G4MP2 calculations and decreased by one third of 19 kcal/mol, which is 6.3 kcal/mol.

Table S5: Length of MD simulation runs

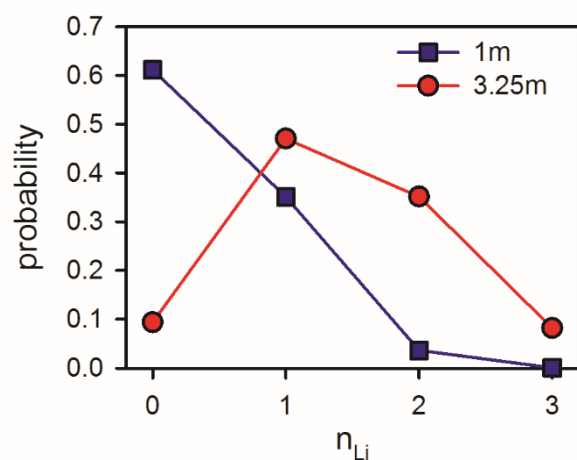| T (K)	363	333	298	363	333	298
equilibration run (ns)	10.0	10.73	10.5	10	20	22
production run (ns)	10.16	19	19.2	19	23.4	29.5

Figure S27: Probability of finding n_{Li} cations within the first coordination shell of N(FSI) from MD simulations of LiFSI-SL at 298 K. The first coordination shell size was chosen as 5 Å to encompass the first peak of the Li-N(FSI) radial distribution functions shown in Figure S21.
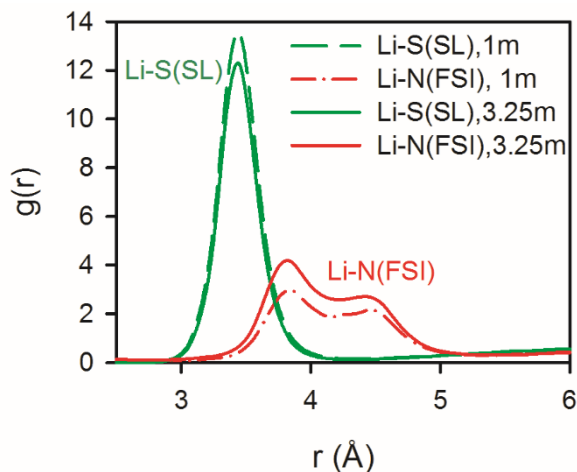
Figure S28: Radial distribution functions from MD simulations at 298 K for the Li^+ cation with S of SL and N of FSI.

DFT Studies of SL De-hydroxylation on Cathode Surface

Periodic planewave DFT+U calculations for the electrolyte/cathode interface systems were performed using the Vienna ab initio Simulation Package (VASP) with the spin-polarized Perdew-Burke-Ernzerhof (PBE) exchange-correlation functional and the projector- augmented wave (PAW) scheme to treat core electrons.[15-22] VASP standard pseudopotentials (PP) were used for carbon, oxygen, sulfur, nitrogen, fluorine, and hydrogen atoms. The PAW PPs employed for the transition metal atoms Ni and Mn (denoted as Ni_pv and Mn_pv, respectively) treat p semi-core states as valence states. The Li_sv PP used for Li treats the 1s shell as valence states. A planewave energy cutoff of 520 eV was employed. Dipole and quadrupole corrections to the energy were included using a generalized Makov-Payne method as implemented in VASP. For the +U augmented treatment of Ni and Mn 3d orbitals, we chose a U_{eff} value of 5.96 eV for Ni and 4.5 eV for Mn.[23] We adopted the disordered configuration (Fd3m phase) with uniformly distributed Ni and Mn ions. The [111] surface for the fully delithiated ($Ni_{0.5}Mn_{1.5}O_4$) structure was generated by removing the Li atoms from the corresponding fully lithiated ($LiNi_{0.5}Mn_{1.5}O_4$; Li/Ni/O termination) slab structure and re-optimizing. The $Ni_{0.5}Mn_{1.5}O_4$[111] slab consists of 13 layers and an xy-plane of dimensions 23.50 Å x 20.35 Å with 20 Å of vacuum in the z-direction. For the de-lithiated high-voltage spinel, the magnetic ordering changes with respect to the ferrimagnetic state of the fully lithiated structure due to a change in oxidation state of the Ni ions from (II) to (IV). Therefore, we impose a ferromagnetic state for the Mn sub-lattice and a net magnetic moment of zero for the Ni ions. Nudged Elastic Band (NEB) calculations were performed using a 10^{-4} eV convergence criterion and a 2x2x1 Brillouin zone sampling. The three-body based dispersion correction with Becke-Johnson damping, employing Grimme's standalone DFT-D3 code for single point energy calculations, was applied to the NEB-determined reactant, product, and transition state structures to estimate the effect of dispersion on reaction barriers and energies.[24] We used the VASPsol code to determine the effect of solvation on reaction barriers and energies by performing implicit solvent single point energy calculations on the reactant, product, and transition state structures obtained from the NEB calculations.[25]

NEB calculations within the Density Functional Theory (DFT) formalism were performed to determine the deprotonation reaction barrier for the following two different electrolyte/cathode interface systems shown in Figure S22: (1) SL interacting with the fully de-lithiated $Ni_{0.5}Mn_{1.5}O_4$[111] spinel and (2) a complexed cluster consisting of LiFSI-SL interacting with the fully de-lithiated $Ni_{0.5}Mn_{1.5}O_4$[111] spinel. The deprotonation reaction consists of a proton transfer from SL to a nucleophilic surface oxide ion. The two model systems are designed to measure the effect on the reaction energetics of going from a standard concentration LiFSI-SL electrolyte to a superconcentrated LiFSI-SL formulation for the most aggressive oxidative electrochemical environment corresponding to a high state-of-charge. The coordination environment for SL at the cathode interface is expected to be similar to the solvation shell structure characteristics of the LiFSI-SL bulk electrolyte,

where our MD simulations of bulk electrolyte showed that the 1m LiFSI-SL solvent is largely dissociated with 61% free SL and the 3.25m LiFSI-SL solution is highly aggregated with 90% FSI⁻ coordinated to Li⁺. Therefore, the SL/Ni$_{0.5}$Mn$_{1.5}$O$_4$[111] system consisting of an isolated SL molecule mirrors the solvation shell structure of SL in the 1m LiFSI-SL bulk electrolyte, whereas the (LiFSI-SL)/Ni$_{0.5}$Mn$_{1.5}$O$_4$[111] system with a Li⁺ cation coordinated to SL represents the highly aggregated characteristic of the 3.25m LiFSI-SL solvent. From our DFT interface calculations we find that the reaction barrier of 0.51 eV does not change in going from the 1m LiFSI-SL electrolyte to the 3.25m LiFSI-SL electrolyte. In contrast, the reaction energy goes from an exothermic deprotonation of -0.37 eV for the 1m LiFSI-SL model system to a reaction energy of near zero for the superconcentrated 3.25m LiFSI-SL. We find that implicit solvation with a large dielectric constant value of eps=80 applied to the (LiFSI-SL)/Ni$_{0.5}$Mn$_{1.5}$O$_4$[111] interface slightly increases the reaction barrier by 0.12 eV and has a negligible effect on the reaction energy in comparison to the calculations performed under Ultra High Vacuum conditions. The implications of the NEB results in regard to the improved electrochemical performance exhibited by the superconcentrated electrolyte at the LNMO cathode are two-fold. First, the protonation of surface oxide anions would lead to a weakening of the bonds between surface oxygen atoms and the sub-surface Mn ions. Such a weakening of Mn-O bonds may facilitate the transition metal dissolution largely responsible for the severe capacity fade common to the high voltage LNMO cathode. Second, since a proton transfer to the cathode is not energetically favorable for the superconcentrated electrolyte, the competing SL-SL and SL-LiFSI oxidation reactions are expected to dictate the cathode interfacial chemistry. Our QC cluster calculations show that SL-SL and SL-LiFSI interactions undergo energetically favorable propagation and termination reactions conducive to a slow polymerization and passivation layer formation. Thus, the use of the superconcentrated 3.25m LiFSI-SL electrolyte in combination with the high voltage LNMO spinel may help to suppress cathode material degradation and may help to promote the formation of a stable cathode electrolyte interface.
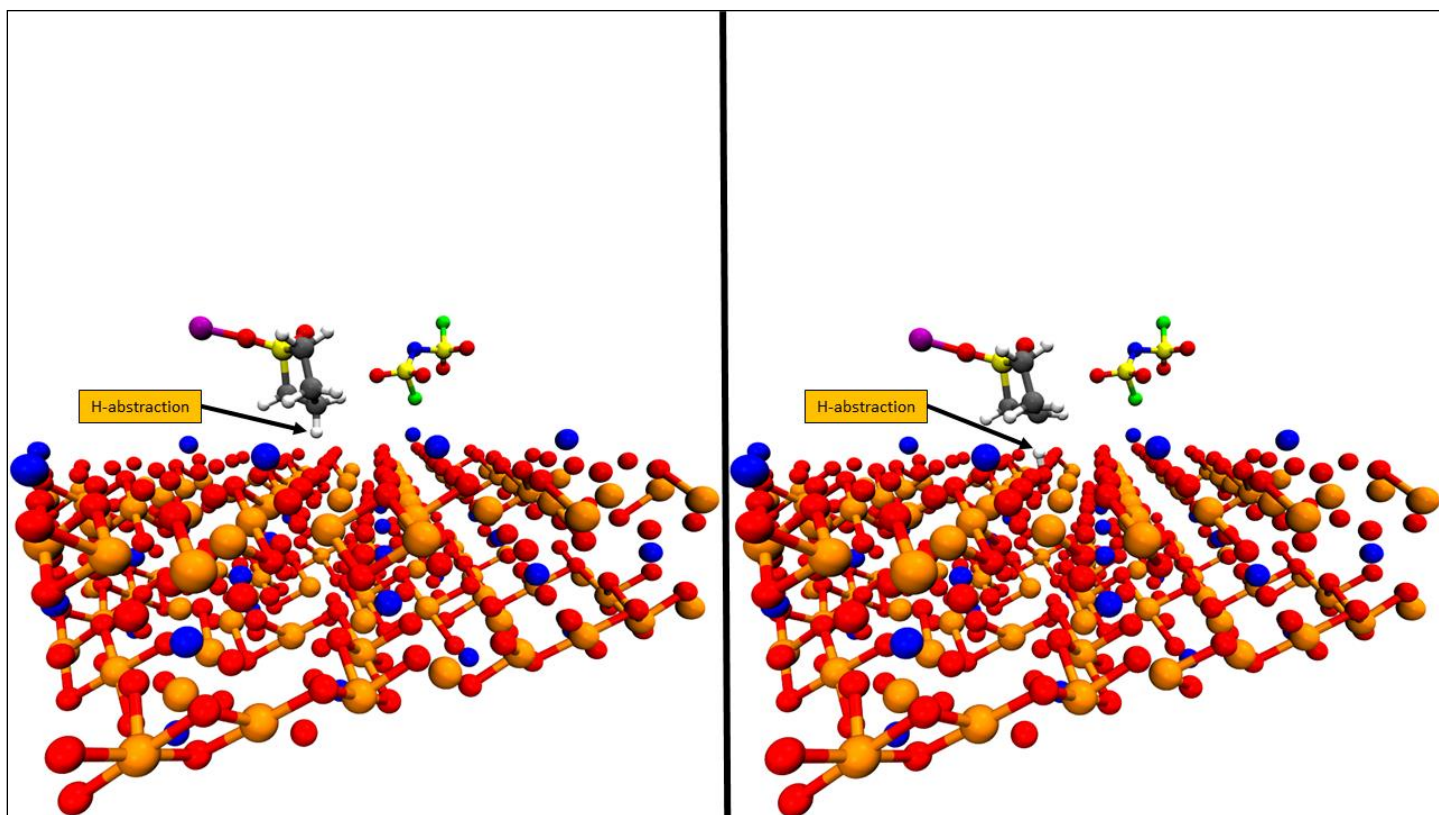

Figure S29. Left panel: Reactant state for the (SL+Li⁺/FSI⁻)/Ni$_{0.5}$Mn$_{1.5}$O$_4$[111] system with a Li⁺ coordinated to a SL oxygen atom. Right panel: Product state for the (SL+Li⁺/FSI⁻)/Ni$_{0.5}$Mn$_{1.5}$O$_4$[111] system after the proton abstraction reaction. The interface model for the SL/Ni$_{0.5}$Mn$_{1.5}$O$_4$[111] system is very similar but does not include Li⁺ and FSI

SI References

[1] Y. Pan, G.L. Wang, B.L. Lucht, Electrochim Acta, 217 (2016) 269-273.

[2] M. Nie, D.P. Abraham, D.M. Seo, Y. Chen, A. Bose, B.L. Lucht, The Journal of Physical Chemistry C, 117 (2013) 25381-25389.

[3] K. Xu, Journal of the Electrochemical Society, 156 (2009) A751-A755.

[4] H. Bryngelsson, M. Stjerndahl, T. Gustafsson, K. Edström, J Power Sources, 174 (2007) 970-975.

[5] Q. Zhang, J.J. Chen, X.Y. Wang, C. Yang, M.S. Zheng, Q.F. Dong, Phys Chem Chem Phys, 17 (2015) 10353-10357.

[6] S. Li, X. Xu, X. Shi, B. Li, Y. Zhao, H. Zhang, Y. Li, W. Zhao, X. Cui, L. Mao, J Power Sources, 217 (2012) 503-508.

[7] B. Philippe, R.m. Dedryvère, M. Gorgoi, H. Rensmo, D. Gonbeau, K. Edström, Journal of the American Chemical Society, 135 (2013) 9829-9842.

[8] W. Gu, O. Borodin, B. Zdyrko, H.-T. Lin, H. Kim, N. Nitta, J. Huang, A. Magasinski, Z. Milicev, G. Berdichevsky, G. Yushin, Adv. Func. Mater., 26 (2016) 1490-1490.

[9] Z. Lu, L. Yang, Y. Guo, J Power Sources, 156 (2006) 555-559.

[10] A. Hammami, N. Raymond, M. Armand, Nature, 424 (2003) 635.

[11] O. Borodin, G.D. Smith, J. Phys. Chem. B, 113 (2009) 1763-1776.

[12] L. Suo, O. Borodin, T. Gao, M. Olguin, J. Ho, X. Fan, C. Luo, C. Wang, K. Xu, Science, 350 (2015) 938-943.

[13] O. Borodin, J. Phys. Chem. B, 113 (2009) 11463-11478.

[14] C.W. Bauschlicher, J.B. Haskins, E.W. Bucholz, J.W. Lawson, O. Borodin, J. Phys. Chem. B, 118 (2014) 10785-10794.

[15] P.E. Blochl, Physical Review B, 50 (1994) 17953-17979.

[16] G. Kresse, J. Furthmuller, Computational Materials Science, 6 (1996) 15-50.

[17] G. Kresse, J. Furthmuller, Physical Review B, 54 (1996) 11169-11186.

[18] G. Kresse, J. Hafner, Physical Review B, 47 (1993) 558-561.

[19] G. Kresse, J. Hafner, Physical Review B, 49 (1994) 14251-14269.

[20] G. Kresse, D. Joubert, Physical Review B, 59 (1999) 1758-1775.

[21] J.P. Perdew, K. Burke, M. Ernzerhof, Physical Review Letters, 77 (1996) 3865-3868.

[22] J.P. Perdew, K. Burke, M. Ernzerhof, Physical Review Letters, 78 (1997) 1396-1396.

[23] F. Zhou, M. Cococcioni, C.A. Marianetti, D. Morgan, G. Ceder, Physical Review B, 70 (2004).

[24] S. Grimme, J. Antony, S. Ehrlich, H. Krieg, Journal of Chemical Physics, 132 (2010).

[25] K. Mathew, R. Sundararaman, K. Letchworth-Weaver, T.A. Arias, R.G. Hennig, Journal of Chemical Physics, 140 (2014).